PCCP

PAPER

Electrochemical detection of receptor-mediated endocytosis by scanning electrochemical microscopy

Yasufumi Takahashi,*[a] Takeshi Miyamoto,[a] Hitoshi Shiku,*[a] Kosuke Ino,[a] Tomoyuki Yasukawa,[b] Ryutaro Asano,[c] Izumi Kumagai[c] and Tomokazu Matsue*[ad]

We report a scanning electrochemical microscopy (SECM)-based receptor-mediated endocytosis detection method. Epidermal growth factor receptor (EGFR), which is one of the key membrane proteins associated with cancer, was used as a model for receptor-mediated endocytosis. EGFR molecules on the outer cell membrane were detected by SECM by using alkaline phosphatase (ALP) as a labeling enzyme. Since SECM detected the ALP activity on the outer membrane, the procedure helped discriminate the EGFR on the outer membrane from the intracellular EGFR involved in endocytosis. SECM showed a marked decrease in the current responses generated due to ALP activity by 93% on addition of the epidermal growth factor, indicating clearly that EGF triggered the endocytosis, which led to the withdrawal of most EGFRs from the outer membrane.

Introduction

Endocytosis is a process characterized by internalization of extracellular molecules followed by engulfment of these molecules by the cellular membrane to form an endocytic vesicle. Receptor-mediated endocytosis is an important process that negatively regulates the receptor-mediated signals by reducing the surface concentration of the receptor itself (down-regulation) and controls the strength and duration of the signals downstream.[1] Then, the receptor is recycled back to the plasma membrane. Epidermal growth factor receptor (EGFR) is one of the key membrane proteins associated with cancer.[2] Epidermal growth factor (EGF) binds to the EGFR, and the activated EGFR initiates the signaling cascades, thereby promoting cell proliferation, differentiation, apoptosis, and migration. This signaling is controlled by EGF-triggered endocytosis, which reduces the number of EGFR molecules exposed to the outside medium. Therefore, various methods have been established to study endocytosis of EGFR. Fluorescence measurement is an effective method for imaging of the membrane protein, but visualization of the membrane protein motion at the interface of the cellular membrane remains difficult because long-term monitoring of fluorescence signals induces photobleaching.[3] Sokolov and coworkers developed a labeling method for membrane proteins by using anti-EGFR gold nanoparticles for monitoring endocytosis. The absorption wavelengths of the nanoparticles trapped in the vesicle changed according to the interparticle center–center distance; therefore, this method was effective for monitoring the endocytosis process.[4] However, identification of the starting point of vesicle formation is quite difficult. Therefore, development of an analytical tool that allows discrimination of the EGFR molecules on the outer membrane from those of the inner endocytic vesicles is necessary. Korchev and coworkers developed scanning ion conductance microscopy (SICM) for visualizing the surfaces of living cells,[5] and SICM has been reported to be effective for visualizing the endocytic pit.[6]

Scanning electrochemical microscopy (SECM) is a useful tool for analyzing biological samples in a noninvasive manner. Since a localized chemical reaction and chemical concentration near the sample under physiological conditions can be quantitatively and noninvasively characterized as a Faradaic current by scanning the microelectrode, SECM has been applied for quantitative investigation of living cells.[7][9] The application of SECM for investigation of living cells has several advantages. First, SECM can selectively detect the cell membrane protein at the outer membrane surface.[10] In this study, the membrane protein was labeled with an enzyme-labeled antibody. Recently, this method was applied to determine the expression level of membrane glycans.[11] Simultaneous imaging of the inner and outer sides of the cell was performed by fluorescence measurement using an optical fiber electrode.[12] Second, SECM has a high temporal and spatial resolution for monitoring cellular phenomena that occur at various interfaces. Mirkin and coworkers developed a nanoelectrode and inserted the electrode into a cell for estimating the intracellular redox activity.[13]
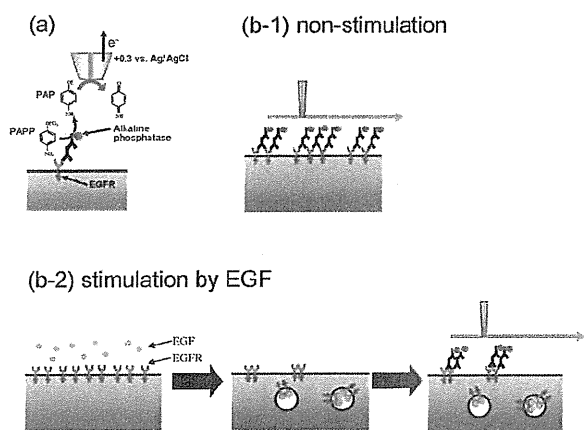
[a] Graduate School of Environmental Studies, Tohoku University, Aramaki, Aoba 6-6-11-605, Sendai 980-8579, Japan. E-mail: yasufumi1981@hotmail.com
[b] Graduate School of Material Science, University of Hyogo, 3-2-1 Kouto, Kamigori-cho, Ako-gun, Hyogo 678-1297, Japan
[c] Graduate School of Engineering, Tohoku University, Aramaki, Aoba 6-6-11-607, Sendai 980-8579, Japan
[d] Advanced Institute of Materials Research, Tohoku University, Katahira, Aoba 2-1-1, Sendai 980-8577, Japan

This journal is © the Owner Societies 2011

Phys. Chem. Chem. Phys., 2011, **13**, 16569–16573 | 16569

Fig. 1 (a) Schematic illustration of EGFR detection using SECM. The EGF stimulation induced endocytosis was estimated by comparing the PAP oxidation current responses of the non-stimulation (b-1) and stimulation by EGF (b-2) cells.

Wightman and coworkers performed real-time monitoring of neurotransmitter release associated with exocytosis.[14] Unwin and coworkers probed the dynamics of partitioning of electro-active solutes between two immiscible phases using SECM.[15] We estimated the degree of cell membrane permeability of the electrochemical mediator by using a microelectrode.[16] Previous studies have shown that SECM is a suitable analytical tool for monitoring various phenomena that occur at the cellular interface. However, SECM monitoring of the membrane protein motion at the cellular interface has not been reported. In this study, we used SECM to investigate EGF-triggered endocytosis (Fig. 1). EGFR was labeled with an alkaline phosphatase (ALP)-labeled antibody for electrochemical detection. The decrease in the expression level of EGFR induced by the EGF-triggered endocytosis was estimated by comparing the Faradaic current responses of the cells with and without EGF stimulation. To the best of our knowledge, this is the first study to report the detection of endocytosis by using SECM.

Experimental

Materials

Primary antibodies (mouse anti-EGFR IgG [SC-120, Santa Cruz Biotechnology, Santa Cruz, CA]), mouse anti-EGFR IgG labeled with fluorescein isothiocyanate (FITC [sc-120 FITC, Santa Cruz Biotechnology, Santa Cruz, CA]), secondary antibodies (goat anti-mouse IgG labeled with ALP [62-6522, Zymed]), Alexa Fluor® 488 EGF complex (E13345) molecular probe, recombinant human epidermal growth factor (BD Biosciences), p-aminophenyl phosphate monosodium salt (PAPP; LKT Lab Inc.), and poly(dimethylsiloxane) (PDMS; Dow Corning Toray Co., Ltd.) were purchased and used as received. All other chemicals were also used as received. All the solutions were prepared using distilled water obtained using a Milli-Q water system (Millipore, Japan).

Cell culture

A normal Chinese hamster ovary (CHO) and cells derived from human epidermoid carcinoma cell line A431 were donated by the

Cell Resource Center for Biomedical Research (Tohoku University). The EGFR/CHO (CHO transfected with EGFR) cells used in this study were prepared according to the literature.[17] Normal CHO and A431 cells were cultured in RPMI-1640 medium (Gibco/Invitrogen, Tokyo, Japan) containing 10% fetal bovine serum (FBS; Gibco), 50 µg mL^{-1} penicillin (Gibco), and 50 µg mL^{-1} streptomycin (Gibco) at 37 °C in a humidified atmosphere containing 5% CO_2. The EGFR/CHO cells were cultured in RPMI-1640 medium (Sigma) containing 10% FBS (Gibco), and 50 µg mL^{-1} G418 (Nacalai Tesque) at 37 °C in a humidified atmosphere containing 5% CO_2.

EGFR labeling for fluorescence measurements

EGFR was visualized with a fluorescent-labeled EGF (Alexa Fluor® 488 EGF complex) or a fluorescent-labeled antibody (anti-EGFR IgG labeled with FITC). For fluorescence labeling, the cells were reacted with RPMI-1640 containing fluorescent-labeled EGF (1 µg mL^{-1}) or a FITC-labeled antibody (1 µg mL^{-1}) for 60 min at 4 °C, followed by thorough washing with RPMI-1640.

EGFR labeling with ALP for electrochemical measurements

EGFR was labeled with an ALP-labeled antibody for electrochemical detection. In the case of EGFR labeling with an ALP-labeled antibody, the cells were reacted with RPMI-1640 containing an anti-EGFR antibody (1 µg mL^{-1}) for 90 min at 37 °C, followed by thorough washing with RPMI-1640. The cells were then reacted with RPMI-1640 containing an ALP-labeled secondary antibody (ALP-labeled IgG) (1 µg mL^{-1}) for 90 min at 37 °C, followed by thorough washing with RPMI-1640.

Preparation of a cell-patterned substrate

Cell patterns were developed using the polydimethylsiloxane (PDMS) microstencil method. Linear (width, 300 µm) and circular (diameter, 500 µm) patterns of the microstencils were prepared using a CO_2 laser beam (Universal Laser Systems, Scottsdale, Arizona, USA). The cells (10^6 cells per mL, 100 µL) were seeded on a 35 mm Petri dish (Falcon), sealed with the PDMS microstencil, and incubated for 2 h to allow the cells to adhere to the dish. The excess nonadherent cells were then removed by washing with RPMI-1640. After incubation with RPMI-1640 for 1 day, the stencil was peeled off from the dish, and SECM measurement was performed.

SECM measurements

The measurements were performed in a 4-(2-hydroxyethyl)-1-piperazineethanesulfonic acid (HEPES)-based saline solution (10 mM HEPES, 150 mM NaCl, 4.2 mM KCl, and 11.2 mM glucose; pH 9.5) containing 4.7 mM PAPP and 10% FBS for detecting the ALP-labeled EGFR. ALP catalyzes the hydrolysis of PAPP to yield p-aminophenol (PAP) as an enzymatic product, which was detected electrochemically using the microelectrode probe of SECM set at +0.30 V vs. Ag/AgCl (Fig. 1a). A disk-type platinum electrode with a 20 µm diameter (Rg 3.0) was used as a SECM microelectrode probe. A fine Pt wire was inserted into a glass capillary, and shielded by thermal fusing of the glass. Finally, the tip of the capillary was carefully polished to give a disk-type microelectrode. Electrochemical current was

16570 | Phys. Chem. Chem. Phys., 2011, 13, 16569–16573

This journal is © the Owner Societies 2011

measured on the basis of a two-electrode configuration by using an Ag/AgCl electrode as the reference electrode. The details of the SECM system have been reported previously.[8]

Results

SECM imaging of cell patterns

SECM is suitable for noninvasive investigation of the activity of patterned biomolecules. In the past, micro-patterned mammalian cells and enzymes were quantitatively characterized by using SECM.[18,19] Previously, we have shown that EGFR at the cell surfaces can be visualized using ALP as a labeling enzyme. In this study, we used a similar method to investigate the EGFR expression level at the surfaces of CHO, EGFR/CHO, and A431 cells patterned on a solid substrate. EGFR was successively labeled with anti-EGFR and ALP-labeled secondary antibodies. Fig. 2 shows the SECM image of these cells with a line-and-space pattern. The probe electrode of SECM was set at a voltage of +0.30 V and scanned at a distance of 20 μm from the dish to detect the oxidation of the PAP delivered from the labeled ALP. The current responses were based on the electrochemical oxidation of PAP at the SECM probe. Since the ALP labeled on EGFR catalyzes the hydrolysis of PAPP to form PAP, the SECM images can indicate the expression levels of EGFR at the cellular surfaces of 3 different cells. A431 cells showed large current responses, and EGFR/CHO cells showed clear responses, while normal CHO cells showed no obvious signals. This result shows good agreement with the previous results.[8]

Influence of pH on endocytosis

The SECM-based measurement of ALP activity was performed in a relatively high pH solution. A previous study had shown
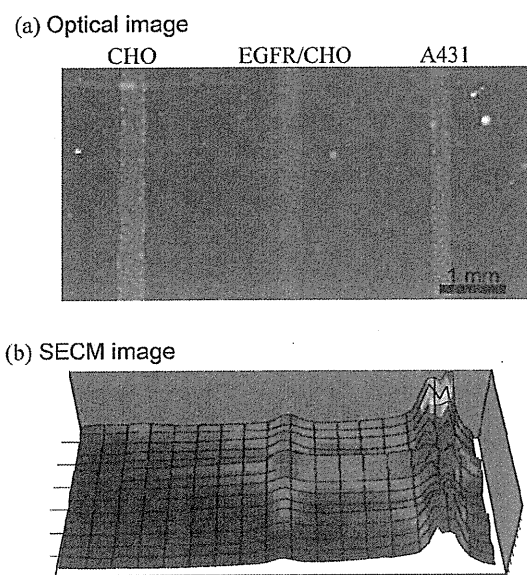
(a) Optical image

(b) SECM image

Fig. 2 SECM image of the EGFR expression level of patterned different kinds of cells. (a) Optical microscopy image, (b) SECM image. The electrode was set at 20 μm above the substrate, and the scan rate was 100 μm s⁻¹. The scan range was 7.0 mm × 3.0 mm, and the step size was 100 μm.
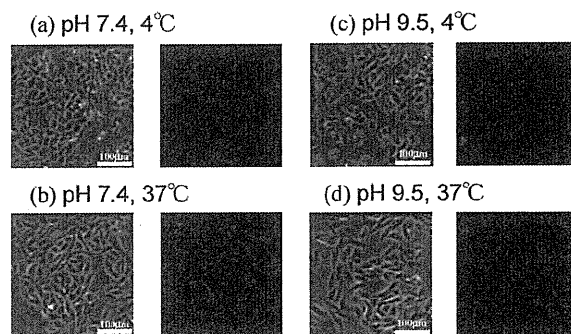

Fig. 3 Investigation of the effect of pH on the EGFR endocytosis. Fluorescent images showed the localization of the EGFR after labelled and stimulated Alexa Fluor® 488 EGF complex. The cells were incubated for 1 hour in phosphate buffer of (a) pH 7.4, 4 °C, (b) pH 7.4, 37 °C, (c) pH 9.5, 4 °C, (d) pH 9.5, 37 °C.

that electrochemical measurement in a solution with pH 9.5 did not cause fatal damage to living cells as long as the measurement period was within several hours.[20] In this study, we investigated the influence of high pH on the endocytosis of living cells by using fluorescent-labeled EGF. The labeled EGF binds to EGFR and triggers endocytosis of the vesicles with EGF–EGFR complexes. Fig. 3 shows the fluorescence images of the cells that were stimulated with EGF and incubated for 1 h in a buffer solution of pH 7.0 or 9.5. When the cells were incubated at 4 °C, clear fluorescence signals were observed on the cell surface [Fig. 3(a) and (c)], indicating that EGFR molecules were present on the cell surface at 4 °C. In contrast, vesicles with high fluorescence intensity were observed inside the cells after incubation for 1 h at 37 °C. Thus, it is obvious that endocytosis does not proceed at 4 °C even in the presence of EGF. Notably, no remarkable differences were observed in the formation of vesicles in the fluorescence images at pH 7.4 and 9.5 [Fig. 3(b) and (d)]. This result indicated that high pH did not influence receptor-mediated endocytosis.

Endocytosis-induced decrease in the EGFR levels at the cell surface

EGF-induced endocytosis promotes changes in the EGFR expression level on the cell surface. This change was measured using fluorescence and electrochemical techniques. In the fluorescence measurements, anti-EGFR IgG labeled with FITC was used to visualize EGFR at the cell surface. In the electrochemical measurements, an ALP-labeled antibody was used to detect EGFR on the cell surface on the basis of electrochemical responses. The cells were incubated with EGF in RPMI-1640 medium for 1 h at 37 °C. After the stimulation with EGF, the EGFR expression levels on the cell surface were detected by fluorescence and electrochemical measurements.

Fig. 4 shows the optical and fluorescence images of EGFR/CHO cells with and without EGF stimulation. Although the EGF-induced change in the cell shape was quite difficult to recognize in the optical image, the fluorescence signal slightly decreased after stimulation with EGF. This decrease was possibly caused by EGF-triggered endocytosis to decrease the levels of EGFR molecules at the cell surface. However,

(a)

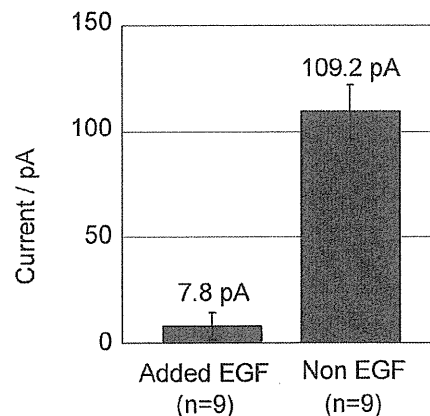Optical image   Fluorescent image

200 μm

(b)

200 um
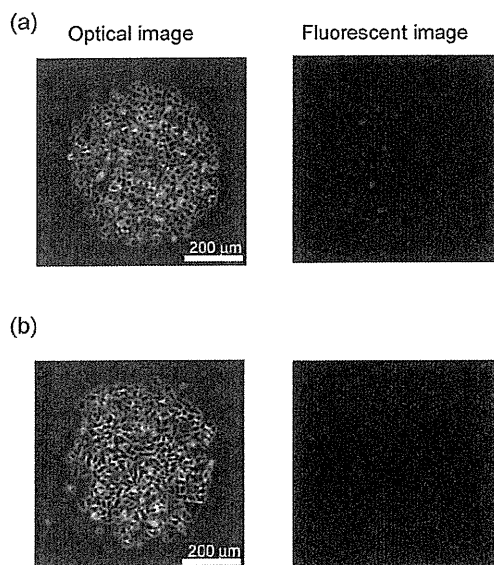
Fig. 4 Investigation of the EGFR expression level of (a) non-stimulated and (b) EGF stimulated EGFR/CHO cells by fluorescent measurement. Fluorescent images showed the expression level of the EGFR. The EGFR was labeled with anti-EGFR IgG FITC conjugated.

although we used confocal microscopy for imaging, it was difficult to discriminate the EGFR on the surface from intracellular EGFR because of the motion of the cellular membrane.

Fig. 5 shows the SECM images of the ALP-antibody-labeled EGFR/CHO cells with and without EGF stimulation together with the corresponding optical images. The labeled ALP catalyzes the hydrolysis of PAPP to yield PAP. The SECM image of cells without the stimulation shows clear responses of the oxidation current at the area of the cell pattern, indicating that SECM can also be used for characterizing the EGFR molecules present on the cell surface. The stimulation with EGF markedly decreased the signal response in the

(a)

Optical image   SECM

200μm

↑ 85 pA ↓

1500×1500 μm

(b)

200μm

↑ 85 pA ↓

1500×1500 μm
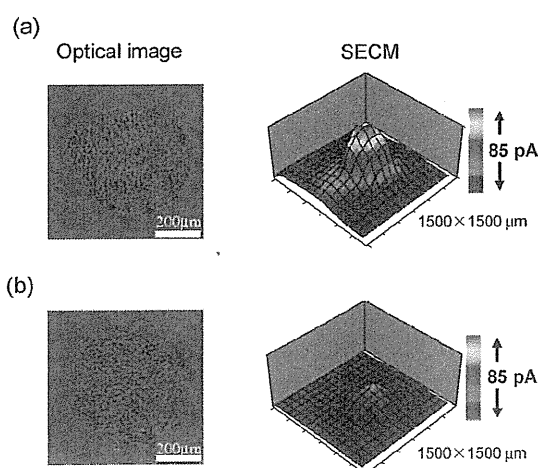
Fig. 5 SECM images of ALP labelled microstencil-patterned EGFR/CHO cells. (a) Non-stimulated and (b) EGF stimulated cells. The electrode was set at 20 μm above the substrate, and the scan rate was 50 m s⁻¹. The scan range was 1500 μm × 1500 μm, and the step size was 50 μm.

150

109.2 pA

100

Current / pA

50

7.8 pA

0

Added EGF   Non EGF
(n=9)   (n=9)

Fig. 6 The current response of EGF stimulated cells and non-stimulated EGFR/CHO cells. The current response was measured by single scan data on the cells pattern.

SECM image. Since the EGFR molecules on the cell surface were detected using SECM, the decrease in the responses indicated the EGF-triggered-endocytosis-induced decrease in the levels of EGFR molecules at the surface. Fig. 6 shows the peak current obtained from the single-scan data on the ALP-antibody-labeled EGFR/CHO cell pattern developed using the previously described procedure.[8] The current responses before and after stimulation with EGF were found to be 109.2 pA and 7.8 pA, respectively. Because of the clear difference in the current responses, we think that SECM measurements are particularly suitable for detecting endocytosis-related events.

Conclusions

In this study, we developed an SECM-based methodology for investigating EGF-triggered endocytosis. This method is suitable for evaluating changes in the EGFR expression level during EGF-triggered endocytosis. SECM enables quantitative evaluation under physiological conditions without having to peel the cells from the culture dish. The current response of the ALP-labeled EGFR/CHO cells investigated using an antibody decreased by 93% after stimulation with EGF. Furthermore, SECM also helped to obtain clear images with adequate spatial and temporal resolutions of the cells before and after occurrence of endocytosis-related events. This methodology is applicable to other biomembrane-related phenomena.

Acknowledgements

Notes and references

1 S. D. Conner and S. L. Schmid, *Nature*, 2003, **422**, 37.
2 K. Roepstorff, L. Grovdal, M. Grandal, M. Lerdrup and B. van Deurs, *Histochem. Cell Biol.*, 2008, **129**, 563.
3 Y. Sako, S. Minoghchi and T. Yanagida, *Nat. Cell Biol.*, 2000, **2**, 168.

4 J. Aaron, K. Travis, N. Harrison and K. Sokolov, *Nano Lett.*, 2009, **9**, 3612.

5 Y. E. Korchev, C. L. Bashford, M. Milovanovic, I. Vodyanoy and M. J. Lab, *Biophys. J.*, 1997, **73**, 653.

6 A. I. Shevchuk, P. Hobson, M. J. Lab, D. Klenerman, N. Krauzewicz and Y. E. Korchev, *Pfluegers Arch.*, 2008, **456**, 227.

7 A. Schulte and W. Schuhmann, *Angew. Chem., Int. Ed.*, 2007, **46**, 8760.

8 A. J. Bard, X. H. Liu, M. M. Ramsey, X. L. Chen, D. Koley and M. Whiteley, *Proc. Natl. Acad. Sci. U. S. A.*, 2011, **108**, 2668.

9 Z. F. Ding, X. C. Zhao, S. Lam and J. Jass, *Electrochem. Commun.*, 2010, **12**, 773.

10 Y. Takahashi, T. Miyamoto, H. Shiku, R. Asano, T. Yasukawa, I. Kumagai and T. Matsue, *Anal. Chem.*, 2009, **81**, 2785.

11 Y. Xue, L. Ding, J. Lei, F. Yan and H. Ju, *Anal. Chem.*, 2010, **82**, 7112.

12 Y. Takahashi, H. Shiku, T. Murata, T. Yasukawa and T. Matsue, *Anal. Chem.*, 2009, **81**, 9674.

13 P. Sun, F. O. Laforge, T. P. Abeyweera, S. A. Rotenberg, J. Carpino and M. V. Mirkin, *Proc. Natl. Acad. Sci. U. S. A.*, 2008, **105**, 443.

14 D. J. Leszczyszyn, J. A. Jankowski, O. H. Viveros, E. J. Diliberto, J. A. Near and R. M. Wightman, *J. Biol. Chem.*, 1990, **265**, 14736.

15 A. L. Barker, J. V. Macpherson, C. J. Slevin and P. R. Unwin, *J. Phys. Chem. B*, 1998, **102**, 1586.

16 H. Yamada, T. Matsue and I. Uchida, *Biochem. Biophys. Res. Commun.*, 1991, **180**, 1330.

17 R. Asano, Y. Sone, K. Makabe, K. Tsumoto, H. Hayashi, Y. Katayose, M. Unno, T. Kudo and I. Kumagai, *Clin. Cancer Res.*, 2006, **12**, 4036.

18 M. Nishizawa, K. Takoh and T. Matsue, *Langmuir*, 2002, **18**, 3645.

19 H. Q. Luo, H. Shiku, A. Kumagai, Y. Takahashi, T. Yasukawa and T. Matsue, *Electrochem. Commun.*, 2007, **9**, 2703.

20 T. Murata, T. Yasukawa, H. Shiku and T. Matsue, *Biosens. Bioelectron.*, 2009, **25**, 913.
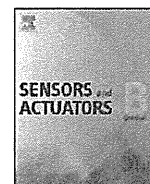
Amperometric detection of DNA hybridization using a multi-point, addressable electrochemical device

Xi Zhu [a,b], Kosuke Ino [b], Zhenyu Lin [a], Hitoshi Shiku [b], Guonan Chen [a], Tomokazu Matsue [b,c,*]

[a] Ministry of Education Key Laboratory of Analysis and Detection for Food Safety, Fujian Provincial Key Laboratory of Analysis and Detection for Food Safety, Department of Chemistry, Fuzhou University, Fuzhou, Fujian 350002, China
[b] Graduate School of Environmental Studies, Tohoku University, 6-6-11-604 Aramaki-Aoba, Aoba, Sendai 980-8579, Japan
[c] Advanced Institute of Materials Research, Tohoku University, 2-1-1 Katahira, Aoba, Sendai 980-8579, Japan

ARTICLE INFO

ABSTRACT

A novel device was designed for the multipoint addressable detection of DNA hybridization. Row and column electrodes array were orthogonally arranged, and the microwells were assembled on the crossing points of the row/column electrodes to form a 4 × 4 microwell array. Amperometric signals at the individual microwells could be detected separately on the basis of redox cycling of localized electroactive species occurring between the electrodes. Immobilization and hybridization of DNA could block the redox cycling of $Fe(CN)_6^{4-}/Fe(CN)_6^{3-}$ at the designated microwells, resulting in the reduction of current response. This device had been used to detect DNA hybridization with excellent sensitivity (0.03 μM) and selectivity. The device can be applied to comprehensive and high-throughput detection and imaging of biochemical species.

1. Introduction

The detection of DNA hybridization is of central importance to the diagnosis and treatment of genetic diseases, for the detection of infectious agents, and for reliable forensic analysis. Hence, various DNA biosensors have been developed based on the immobilization of a single-stranded DNA (ssDNA) probe onto a surface to recognize its complementary DNA target sequence by hybridization. Contrary to DNA biosensors that allow single-shot measurements, DNA arrays allow simultaneous detection and analysis of patterns of expression of thousands of genes in a single experiment [1–4]. Hence, the development of DNA arrays would be more desirable. Because fluorescence measurement usually has a high sensitivity and a variety of tools for performing the measurements are commercially available, many DNA arrays based on fluorescence detection are developed [5–10]. Although DNA arrays based on fluorescence detection are a powerful tool that provides complex and informative data from nucleic acid sequences, they need fluorescence scanners that are inherently costly and not transportable [11], which limited the widespread use of DNA fluorescence arrays for point-of-care testing or as a routine diagnostics tool. Another alternative form of detection utilized in DNA array is electrochemical detection, which possesses the advantages of high sensitivity,

small size, low cost, and compatibility with micromanufacturing technology [12,13]. So far, various DNA arrays based on electrochemical detection have been developed [14–21]. All above arrays were performed by connecting each electrode to a corresponding bond pad in the 1:1 mode. However, the number of individually addressable electrodes is limited, due to sufficient space for bond pads is not available on the chip border.

Recently, a novel multipoint addressable electrochemical device has been reported [22,23]. This device consists of orthogonally arranged arrays of rows and columns of electrodes. Based on the local redox cycling at the crossing points of the row and column electrodes, electrochemical responses at $n \times n$ crossing points were rapidly detected by using only $2n$ bonding pads for the external connection. Based on the detection system, a series of apparatus for biological assay had been developed [23–25]. On the basis of the previous researches [22–25], here, we demonstrate a new amperometric approach for high-throughput detection of DNA hybridization. The principle was based on immobilization and hybridization of DNA inhibited the redox cycling of $Fe(CN)_6^{4-}/Fe(CN)_6^{3-}$ at the designated microwells due to the negatively charged sugar phosphate backbone of DNA [26,27], resulting in decrease of the amperometric signal, and which can be used to assay DNA hybridization. To the best of our knowledge, this is the first report on the amperometric detection of DNA hybridization using this novel multipoint addressable electrochemical device. It is envisioned that this device can be applied to comprehensive and high-throughput detection and imaging of biochemical species.

* Corresponding author at: Advanced Institute of Materials Research, Tohoku University, 2-1-1 Katahira, Aoba, Sendai 980-8579, Japan.
E-mail address: matsue@bioinfo.che.tohoku.ac.jp (T. Matsue).

2. Experimental

2.1. Materials

Capture DNA (sequence: 5'-SH-CCAGTGAGCTTCCCGTTCA-3'), target DNA (sequence: 5'-TGAACGGGAAGCTCACTGG-3') and mismatched probes (sequence: 5'-TTTCCGCTGAGTCCAGATT-3') were bought from Nihon Gene Research Laboratories Inc. DNA solutions were prepared by dissolving DNA into 30 mM pH 7.4 phosphate buffer solutions (PBS) containing 0.1 M NaCl and 5 mM KCl.

Primer and positive photoresist (S1818) were purchased from Shipley Far East Ltd., Japan. Negative photoresist (SU-8 3005) was bought from Nippon Kayaku Co. Ltd., Japan. $K_4[Fe(CN)_6]$ was bought from Wako Pure Chemical Industries, Ltd. All chemicals were used as received, and solutions were prepared using Milli-Q reagent water (Milli-Q, Millipore, 18.2-MΩ resistivity).

2.2. Microelectrode array fabrication

An electrode array was constructed on a glass substrate using a photolithographic method [22,28]. The glass substrates were consecutively cleaned by ultrasonication in acetone and 2-propanol. A primer and positive photoresist were spin-coated at 3000 rpm for 30 s on the glass substrate, followed by baking at 95 °C for 5 min. Then, the substrate was irradiated with UV light for 13 s through a chromium mask with microelectrode patterns. After developing, Ti, Pd and Au were deposited on the substrate by sputtering to create a Ti/Pd/Au multilayer. The electrode pattern was revealed using a lift-off technique by immersing the electrode substrate in an acetone bath, then the substrate was dried to form an electrode array consisting of four microband electrodes (thickness: 300 nm; width: 100 μm; band interval: 900 μm, each electrode). This microelectrode array can be used as the column or row electrodes array due to the different arrangement.

Then four microwells with 100 μm width, 100 μm length, and 5 μm depth, were further fabricated on each column electrode using SU-8 3005 (thickness: 5 μm) on one microelectrode array; thereby, 16 microwells were fabricated on the column-electrode substrate, as shown in Fig. 1A.

2.3. Immobilization and hybridization of DNA on the sensing array

First, the substrates were cleaned before the measurements. Then, the capture DNA was immobilized in the 16 microwells of the column electrode via an Au–S linkage. The column electrode was rinsed carefully with PBS solution. Different concentrations of target DNA were carefully added into the microwells at each of the four corners by the pipette, and incubated for 2 h in a humidified incubator. After these, 4.0 mM $Fe(CN)_6^{4-}$ solution containing 0.1 M KCl was applied to cover the column electrode surface and filled in every microwell. Then another microelectrode array (worked as row electrode) without assemble of microwells was carefully attached orthogonally on the column-electrode substrate face-to-face with double-sided adhesive paper (thickness, 10 μm; Lintec Co., Japan) in order to assemble the microelectrode/microwell array with microwells arranged at the 16 crossing points. Thus a device is obtained, as shown in Fig. 1B.

2.4. Instrumentation

The detection system is shown in Fig. 2A. Three channels (W1–W3) of a multichannel potentiostat (HA-1010 mM4, Hokuto Denko, Corp., Tokyo, Japan) were used for potential control and current acquisition. The potentiostat was connected to the electrodes by a multiplexer, and the data were controlled and collected by a program developed by LabVIEW through an AD/DA converter (PXI-2529 and PXI-6723, respectively, National Instrument, Austin, TX). An Ag/AgCl and a Pt wire were used as the reference and counter electrodes, respectively.

2.5. Amperometric scanning procedure

The reference and counter electrode were laid near the device, as shown in Fig. 1C. Electrochemical detection was performed as follows: a voltage (V_C = 0.0 V) was applied to all the column electrodes through W1 of the potentiostat. At the same time a different voltage (V_R = 0.6 V) was applied to row electrode 1 (R1) through W3 of the potentiostat for 2 s to precondition the system and stabilize the current, while the other row electrodes (R2–R4) were set at V_C through W1. Then, column electrode 1 (C1) was connected to W2 set at V_C, and the current data were transferred to a PC. This read-out process was sequentially repeated from C1 to C4 with a read-out time interval of 20 ms in each step. All the current responses through W2 were read out, while W1 was used only for potential control. Since all row electrodes were connected to W1 (set at V_C) during the above process, no redox cycling was expected at the crossing points on R2–R4 during scanning. The same measurements were sequentially repeated for the other row electrodes (R2–R4) to address and acquire all the responses at every crossing point. The total detection time for the 16 addressing points was less than 9 s.

## 3. Results and discussion

3.1. Principle of detection

The principle of multipoint detection of DNA hybridization is shown in Fig. 3(A). When redox compounds showing reversible electrochemical behavior, such as $Fe(CN)_6^{4-}/Fe(CN)_6^{3-}$, are present in the interspaces between the column and row electrodes, redox cycling between the column and row electrodes proceeds only at crossing points set at appropriate potentials, and amplifies the electrochemical signal. The efficiency of the redox cycling is sensitive to the presence of molecules at the electrode surface. DNA hybridization at the electrode surface partially blocks the redox cycling, thereby decreasing the electrochemical responses.

Fig. 3(B) shows the reduction current at column electrodes with a bare surface, with immobilized probe DNA, and with hybridized DNA in a 4.0 mM $Fe(CN)_6^{4-}$ solution. When the potential of the row electrode was stepped from 0.0 V to 0.6 V, redox cycling of $Fe(CN)_6^{4-}/Fe(CN)_6^{3-}$ proceeded between the row and column electrodes. The reduction current of $Fe(CN)_6^{3-}$ at the column electrode increased rapidly after the potential step and soon showed a steady-state. The level of steady-state current became lower when the column electrode was modified with probe DNA (curve b). A further decrease was observed after hybridization (curve c). Formation of the negatively charged sugar phosphate backbone of DNA at the electrode surface reduces the efficiency of redox cycling of $Fe(CN)_6^{4-}/Fe(CN)_6^{3-}$, resulting in a decrease in the current signals, and thereby allowing the detection of specific DNAs.

3.2. Electrochemical imaging and detection

Capture DNA was immobilized in all 16 microwells via a thiol–Au linkage. Then, different concentrations (0.05, 0.1, 0.5, and 1 μM) of target DNA solution were added to the microwells at the four corners (A, B, C and D, respectively), as shown in Fig. 4(A). Because the gap between the row and column electrodes is 10 μm, redox cycling was expected [29] and the reduction current was acquired, and which can amplify the current responses [30]. Fig. 4(B) is the amplified amperometric imaging of the 16 microwells, which clearly shows that the responses at the four corners are
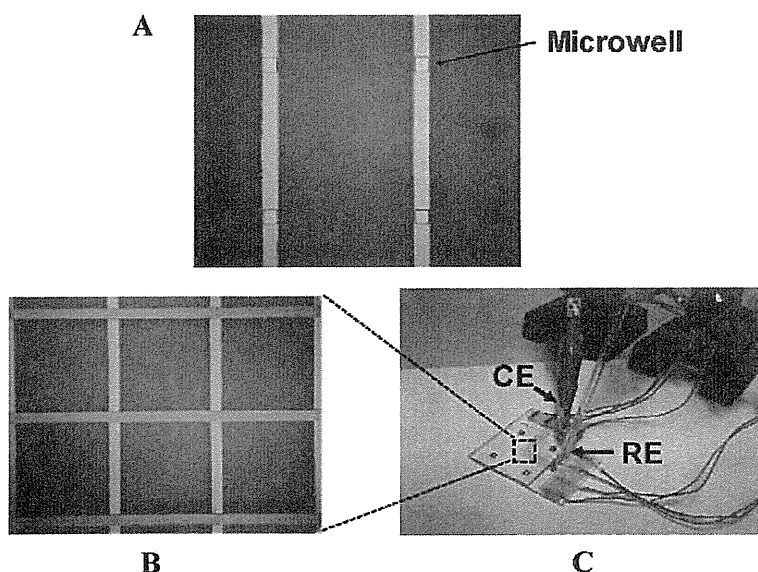
Fig. 1. Optical photographs of (A) the row electrode with microwells, (B) the device consisted of orthogonally arranged arrays of rows and columns of electrodes, and (C) the use of the device with reference electrode (RE) and counter electrode (CE).
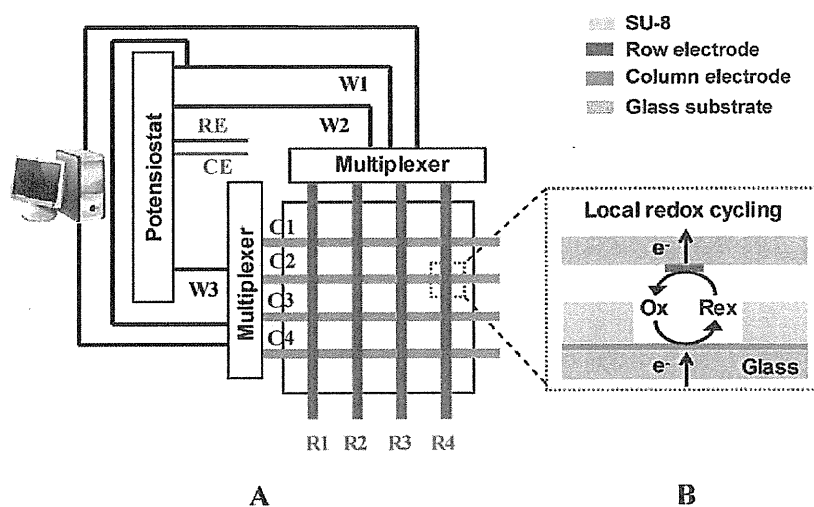
Fig. 2. (A) Schematic diagram of the addressable microelectrode array detection system. The dashed part represents the working area of the device viewed from the top. (B) Side view of a crossing point. Local redox cycling occurs at the crossing points of the column and row electrodes.

lower than those of other areas, indicating that dsDNA efficiently inhibits the redox cycling of $Fe(CN)_6{}^{4-}/Fe(CN)_6{}^{3-}$ in the microwells located at the crossing points of the row and column electrodes. It is also found that the response decreases with increasing concentration of target DNA, as shown in Fig. 4(C). The responses show obvious concentration dependence in the range of 0.05 ~ 1 μM. The linear range of this array is wider than the published one [19]. And this DNA array has a detection limit of 0.03 μM (defined as S/N = 3), which is similar to the previous report [31].

3.3. Specificity and reproducibility of the microelectrode

We also investigated the influence of a mismatched probe (1 μM, sequence: 5'-TTTCCGCTGAGTCCAGATT-3'). Capture DNA was chemically immobilized by a thiol–Au linkage in eight microwells, then the target DNA or mismatched DNA was added to the designated microwells shown in Fig. 5(A). Fig. 5(B) shows the histogram of the amplified current responses at different crossing

points modified with different DNAs. Immobilization of capture DNA in the microwells decreased the current responses, whereas no decrease in the current signal was observed when the target DNA was added into bare microwells. This result indicates that the target DNA does not physically adsorb onto the microwells. A significant decrease in the current responses was observed when the target DNA was introduced into the capture DNA-immobilized microwells. On the other hand, the presence of the mismatched DNA only led to a slight decrease in the current response. The above results demonstrate that this device can be used for multipoint addressable detection of DNAs with well specificity.

Additionally, the untapped devices are used to repeat above modified process (immobilization and hybridization of DNA) and electrochemical experiment. It is found that current responses in each microwells changed ±4%. And after the repeated measurement (10 times), the current responses kept about 95%, which shows this DNA array has well reproducibility and stability.
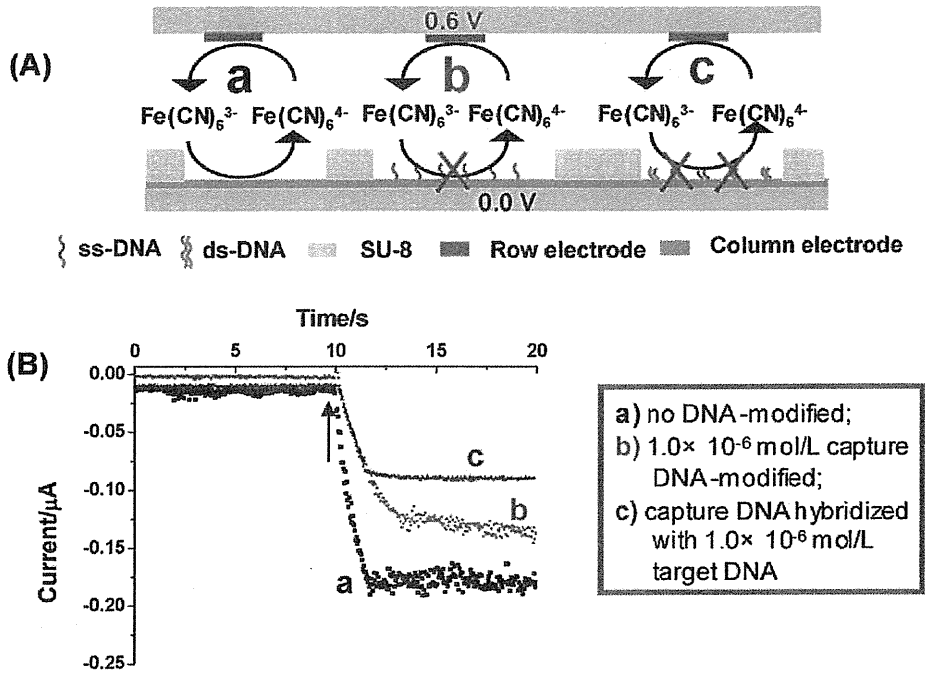
Fig. 3. (A) Principle of multipoint detection of DNA hybridization. (B) Amperometric responses at different gold microelectrodes; curves a, b, and c are the bare gold microelectrode, the ssDNA-modified, and the dsDNA-modified microelectrode, respectively. The potential of the row electrode was stepped from 0.0 V to 0.6 V at the point indicated by the arrow.
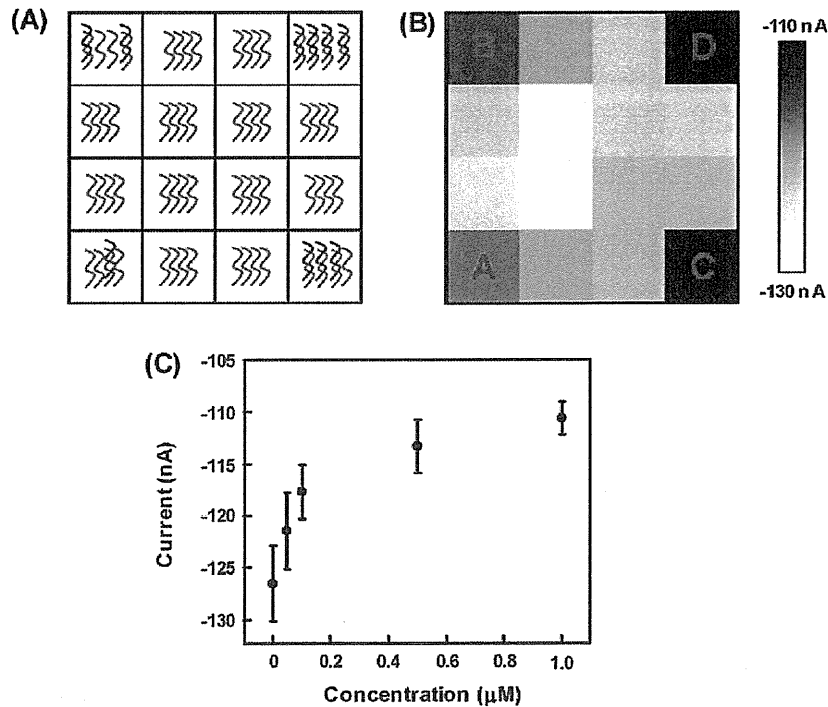

Fig. 4. Detection of DNA hybridization. (A) Schematic of the modification of DNA, and (B) imaging of the amplified reduction current responses at the 16 crossing points. The capture probes were modified at all crossing points, and different concentrations (0.05, 0.1, 0.5, and 1 μM) of target DNA were modified at the four corners (A, B, C, and D, respectively). (C) The relationship between different concentrations of target DNA and reduction currents. Data points represent means ± SD of three independent experiments.

3.4. Prospect of this device

Based on above results, it is envisioned that this device has applications in high-throughput DNA assays, such as DNA diagnostics, gene analysis, fast detection of biological warfare agents, and forensic applications. For example, it can be used to simultaneous detection of the HIV-1 and HIV-2 oligonucleotides [19] and different food-contaminating pathogenic bacteria [20].

Although the present method is suitable for high-throughput DNA assays, the present method may be unsuitable for highly
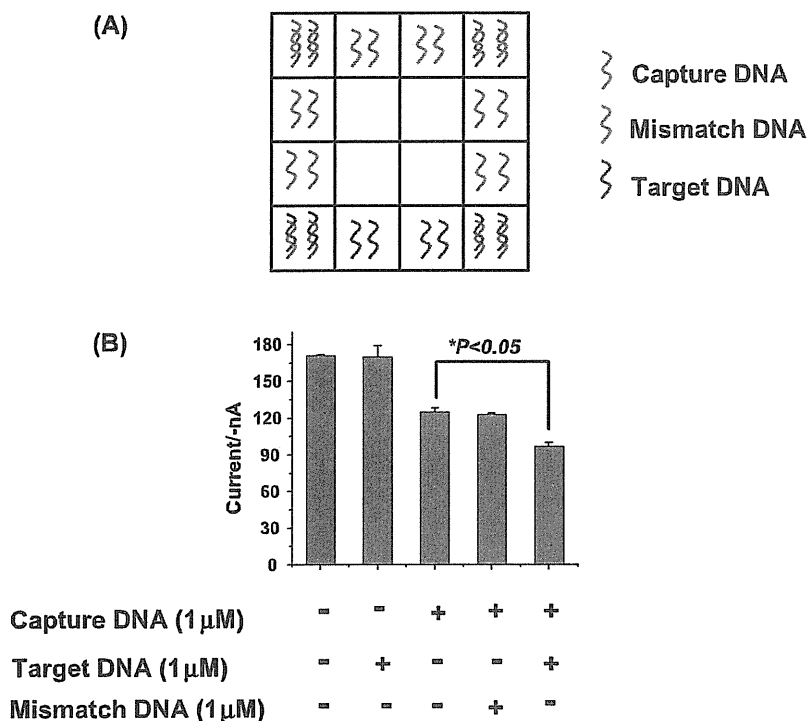
Fig. 5. (A) Schematic diagram of the crossing points modified with different DNAs. (B) Histogram of the amplified reduction current responses at different crossing points modified with different DNAs. The columns from left to right are the currents of the microwells without DNA, with modified-target DNA, with modified-capture DNA, with modified-(capture DNA + mismatched DNA), and with modified-(capture DNA + target DNA). The concentrations of capture DNA, target DNA, and mismatched DNA were 1 μM. Data points represent means ± SD of three independent experiments.

sensitive DNA detection (e.g. detection of DNA in blood) because the sensitivity of the present device is not very high compared to that of conventional methods (e.g. fluorescence and PCR methods). We think that this kind of device can be used for a simple test for a sample with large amounts of DNA fragments. It is necessary to improve the sensitivity for a detailed analysis. It is important for improving the sensitivity of the assay to reduce the gap between the row electrode and column electrode and to amplify electrochemical signals. Wolfrum et al. have reported over 1000-fold electrochemical signal amplification based on rapid redox cycling between plane parallel electrodes inside a nanochannel (height, 55 nm) [32]. Therefore, it is expected to amplify significantly electrochemical signals by reducing the gap between the row electrode and column electrode of the present device.

4. Conclusions

We have devised a high-throughput amperometric DNA assay using a novel addressable electrochemical device. Immobilization and hybridization of DNA in microwells decrease the amperometric responses from redox cycling at the crossing points of row and column electrodes. The observed current decrease demonstrates that we have successfully performed multipoint, and addressable detection of target DNA. Additionally, this device has good selectivity to specific DNA. This methodology will afford an inexpensive platform for comprehensive, high-throughput assays in clinical diagnosis.

Acknowledgments

References

[1] J. Lamartine, Materials Science and Engineering C 26 (2006) 354–359.
[2] F. Bertucci, R. Houlgatte, C. Nguyen, P. Viens, B. Jordan, D. Birnbaum, The Lancet Oncology 2 (2001) 674–682.
[3] P. Bryant, D. Venter, R. Robinsbrowne, N. Curtis, The Lancet Infectious Diseases 4 (2004) 100–111.
[4] C.C. Xiang, Y. Chen, Biotechnology Advances 18 (2000) 35–46.
[5] J.M. Moran-Mirabal, C.P. Tan, R.N. Orth, E.O. Williams, H.G. Craighead, D.M. Lin, Analytical Chemistry 79 (2007) 1109–1114.
[6] K.D. Barbee, X. Huang, Analytical Chemistry 80 (2008) 2149–2154.
[7] J. Kim, R.M. Crooks, Analytical Chemistry 79 (2007) 7267–7274.
[8] F.J. Steemers, J.A. Ferguson, D.R. Walt, Nature Biotechnology 18 (2000) 91–94.
[9] H.A. Behrensdorf, M. Pignot, N. Windhab, A. Kappel, Nucleic Acids Research 30 (2002) e64.
[10] J.R. Epstein, A.P.K. Leung, K.-H. Lee, D.R. Walt, Biosensors and Bioelectronics 18 (2003) 541–546.
[11] S.J. Lassiter, W.J. Stryjewski, Y. Wang, S.A. Soper, Spectroscopy 17 (2002) 14–23.
[12] S.-J. Park, T.A. Taton, C.A. Mirkin, Science 295 (2002) 1503–1506.
[13] A. Sassolas, B.D. Leca-Bouvier, L.J. Blum, Chemical Reviews 108 (2008) 109–139.
[14] Y. Huang, K.L. Ewalt, M. Tirado, R. Haigis, A. Forster, D. Ackley, M.J. Heller, J.P. O'Connell, M. Krihak, Analytical Chemistry 73 (2001) 1549–1559.
[15] D. Xu, D. Xu, X. Yu, Z. Liu, W. He, Z. Ma, Analytical Chemistry 77 (2005) 5107–5113.
[16] L. Niu, W. Knoll, Analytical Chemistry 79 (2007) 2695–2702.
[17] H. Li, Z. Sun, W. Zhong, N. Hao, D. Xu, H.-Y. Chen, Analytical Chemistry 82 (2010) 5477–5483.
[18] R. Kalantari, R. Cantor, H. Chen, G. Yu, J. Janata, M. Josowicz, Analytical Chemistry 82 (2010) 9028–9033.
[19] D. Zhang, Y. Peng, H. Qi, Q. Gao, C. Zhang, Biosensors and Bioelectronics 25 (2010) 1088–1094.
[20] F. Farabullini, F. Lucarelli, I. Palchetti, G. Marrazza, M. Mascini, Biosensors and Bioelectronics 22 (2007) 1544–1549.
[21] Y.-S. Choi, K.-S. Lee, D.-H. Park, Journal of Micromechanics Microengineering 15 (2005) 1938–1946.
[22] Z. Lin, Y. Takahashi, Y. Kitagawa, T. Umemura, H. Shiku, T. Matsue, Analytical Chemistry 80 (2008) 6830–6833.
[23] Z. Lin, Y. Takahashi, T. Murata, M. Takeda, K. Ino, H. Shiku, T. Matsue, Angewandte Chemie International Edition 48 (2009) 2044–2046.

[24] Z. Lin, K. Ino, H. Shiku, T. Matsue, Chemical Communications 46 (2010) 559–561.
[25] Z. Lin, K. Ino, H. Shiku, T. Matsue, G. Chen, Chemical Communications 46 (2010) 243–245.
[26] B. Lillis, M. Manning, E. Hurley, H. Berney, R. Duane, A. Mathewson, M.M. Sheehan, Biosensors and Bioelectronics 22 (2007) 1289–1295.
[27] H. Peng, C. Soeller, N.A. Vigar, V. Caprio, J. Travas-Sejdic, Biosensors and Bioelectronics 22 (2007) 1868–1873.
[28] K. Ino, H. Shiku, F. Ozawa, T. Yasukawa, T. Matsue, Biotechnology and Bioengineering (2009) 709–718.
[29] S.K. Kim, P.J. Hesketh, C. Li, J.H. Thomas, H.B. Halsall, W.R. Heineman, Biosensors and Bioelectronics 20 (2004) 887–894.
[30] T. Yasukawa, K. Nagamine, Y. Horiguchi, H. Shiku, M. Koide, T. Itayama, F. Shiraishi, T. Matsue, Analytical Chemistry 80 (2008) 3722–3727.
[31] O.Y.F. Henry, J.L. Acero Sanchez, D. Latta, C.K. O'Sullivan, Biosensors and Bioelectronics 24 (2009) 2064–2070.
[32] B. Wolfrum, M. Zevenbergen, S. Lemay, Analytical Chemistry 80 (2008) 972–977.

Biographies

Xi Zhu received his BS degree in 2006 from Fujian Normal University, China. Currently, he is studying for the degree of PhD in Fuzhou University, China.

Kosuke Ino received his PhD degree in Engineering from Nagoya University in 2008. He received Research Fellow of the Japan Society for the Promotion of Science (2006–2008). He is currently working as an assistant professor in Graduate School of Environmental Studies, Tohoku University.

Zhenyu Lin received his PhD in analytical chemistry from Fuzhou University in 2007. He is currently working as an associate professor in Department of Chemistry, Fuzhou University.

Hitoshi Shiku received his PhD in Engineering from the Tohoku University in 1997. He is currently working as an associate professor in Graduate School of Environmental Studies, Tohoku University.

Guonan Chen received his BS degree and MS degree from Fuzhou University, China in 1975 and 1982, respectively, and received his PhD from LA TROBE University, Australia in 1990. He is currently a professor in Fuzhou University, China.

Tomokazu Matsue received his PhD in pharmacy from Tohoku University in 1981. He is currently working as a professor in Advanced Institute of Materials Research (WPI-AIMR) and an adjunct professor in Graduate School of Environmental Studies, Tohoku University.

ELSEVIER

Original Article

Myomectomy Decreases Abnormal Uterine Peristalsis and Increases Pregnancy Rate

Osamu Yoshino, MD, PhD*, Osamu Nishii, MD, PhD, Yutaka Osuga, MD, PhD,
Hisanori Asada, MD, PhD, Shigeo Okuda, MD, PhD, Makoto Orisaka, MD, PhD,
Masaaki Hori, MD, PhD, Toshihiro Fujiwara, MD, PhD, and Toshihiko Hayashi, MD, PhD

From the Department of Obstetrics and Gynecology, University of Tokyo (Drs. Yoshino and Osuga), Department of Obstetrics and Gynecology (Dr. Asada),
Department of Radiology, Keio University (Dr. Okuda), Department of Radiology, Juntendo University (Dr. Hori), Reproduction Center, Sanno Hospital (Dr.
Fujiwara), Tokyo, Departments of Obstetrics and Gynecology (Drs. Yoshino and Nishii), Radiology (Dr. Hayashi), Mizonokuchi Hospital, Teikyo University,
Kanagawa, and Department of Obstetrics and Gynecology, University of Fukui (Dr. Orisaka), Fukui, Japan.

ABSTRACT   Background: The relationship between fibroids and infertility remains a critical and unresolved question. During the implan-
tation phase, it is known that uterine peristalsis is dramatically reduced, which is thought to facilitate implantation of the
embryo to the endometrium. In the previous study, using a cine MRI mode, we found that less than half of the patients with
intramural fibroids exhibited abnormal uterine peristalsis during the mid-luteal phase. In the present study, we further inves-
tigated whether myomectomy for patients in the high peristalsis group is a constructive method to normalize uterine peristalsis.
Methods: The frequency of junctional zone movement was evaluated using a cine MRI mode during the mid-luteal phase.
Fifteen infertility patients, who had intramural myomas and exhibited abnormal uterine peristalsis (≥ 2 times/3 min) in their
first MRI, underwent myomectomy and a second MRI. After receiving the second MRI, patients underwent infertility treat-
ment for at least 8 months, and pregnancy rate was evaluated prospectively.
Results: Among 15 patients, the frequency of uterine peristalsis was normalized (0 or 1 time/3min) in 14 patients. Following
myomectomy and second MRI test, 6 of the 15 patients achieved pregnancy (n = 15, pregnancy rate: 40%).
Conclusions: The presence of uterine fibroids might induce abnormal uterine peristalsis in some patients, leading to infertil-
ity, and myomectomy may improve fertility in these patients. Journal of Minimally Invasive Gynecology (2012) 19, 63–67
© 2012 AAGL. All rights reserved.

Keywords: Uterine fibroma; Cine MRI; Uterine peristalsis; Infertility; Myomectomy

DISCUSS   You can discuss this article with its authors and with other AAGL members at
             http://www.AAGL.org/jmig-19-1-11-00328

The relationship between myomas and infertility remains
a critical and unresolved question. Uterine myomas are
grouped according to location: submucous, intramural, or

subserosal. It is generally accepted that the anatomic loca-
tion of a uterine myoma is an important factor in determining
a patient's course of treatment [1]. Meta-analyses have
consistently demonstrated a detrimental effect of submuco-
sal, but not subserosal, myomas on treatment outcomes.
However, conclusions regarding intramural myomas are
conflicting [1,2]. Moreover, because the pregnancy rate
after myomectomy of intramural myomas has varied
widely among previous studies, firm conclusions on the
significance of myomectomy on fertility cannot be drawn
[2]. Therefore management of intramural type myomas con-
tinues to be difficult. To address this problem, we focused on
the mechanisms through which intramural myomas may in-
fluence fertility. It is believed that myomas might interfere

with the process of embryo implantation [3]. This detrimental effect on implantation may be mediated by the occurrence of abnormal uterine contractility [2,4].

During the implantation phase, it is known that uterine peristalsis is dramatically reduced, which is believed to facilitate implantation of the embryo to the endometrium. In a previous study, we examined the frequency of uterine peristalsis with a cine magnetic resonance imaging (MRI) mode display [5]. Among 51 patients with infertility harboring intramural myomas, 22 patients (43%) exhibited a high frequency of uterine peristalsis ($\geq$2 times/3 min), whereas 29 patients (56%) exhibited a low frequency of peristalsis (0 or 1 time/3 min) during the implantation phase. Moreover, after the MRI examination, 10 of 29 patients (34%) with uterine myomas in the low-frequency group achieved pregnancy, whereas none of 22 patients (0%) in the high-frequency group achieved pregnancy, implying that abnormal peristalsis of patients with uterine myomas plays a role in infertility. After our first study, some of the patients with uterine myomas who did not achieve pregnancy underwent myomectomy. In this study, we examined the effect of myomectomy on uterine peristalsis and pregnancy rate in patients with high peristalsis.

Materials and Methods

The inclusion criteria for this study were as follows: (1) Patients who were infertile for at least 24 months with intramural uterine myomas. The patients who had severe symptoms related to myomas were recruited to this study if their infertility period was longer than 12 months; (2) Patients who had no other significant infertility factors in the screening test, such as anovulation, corpus luteum insufficiency, tubal disease, or abnormal semen analysis of the partner; (3) Patients who underwent myomectomy; (4) Patients who underwent MRI before and after myomectomy (referred to as first and second MRI, respectively) and during the time of implantation window (luteal phase day 5–9) and who exhibited abnormal uterine peristalsis with a frequency of uterine peristalsis that was $\geq$2 times/3 min before surgery.

In detail, the patients had regular menstrual cycles of about 28 days. Their basal levels of serum follicle-stimulating hormone, leutinizing hormone and prolactin on menstrual cycle days 3 to 5 were within normal range (criteria: follicle-stimulating hormone 3.5–12.5 mIU/mL, leutinizing hormone 2.4–12.6 mIU/mL, and prolactin 4.9–29.3 ng/mL). Their serum estradiol and progesterone concentrations in the midluteal phase were greater than 100 pg/mL and 10 ng/mL, respectively. The patients had no tubal obstruction detected on hysterosalpingography. Sperm concentration of the partner was at a level greater than 20 $\times$ 10⁶/mL (World Health Organization, 1992). After screening tests were performed, ovarian functional status was monitored predominantly by basal body temperature (BBT) chart. Ovulation was determined by analysis of BBT graphs, wherein a rise in temperature of at least 0.2° C above the preceding 6 days that was completed in

less than 48 hours and sustained for at least 11 days indicated that ovulation had occurred [6]. All patients included in this study showed unequivocal biphasic cycles in their BBT chart. We designated the day showing elevated temperature of at least 0.2° C as luteal phase day 1. MRI was performed before and after myomectomy during the time of implantation window (luteal phase days 5–9), judged retrospectively by BBT chart (evaluated by gynecologists O.Y., T.H.). The conditions for cine mode have been described elsewhere [5,7]. MRI studies were performed with a 1.5-T magnet unit (MRI machine from Siemens Medical Systems at Takinogawa Clinic or from GE Healthcare at Teikyo University) with a 6-ch array coil. Under quiet respiration, a total of 30 serial images were obtained by single-shot fast spin-echo sequence (echo time and repetition time [TR/TE] = 6000/78 msec, field of vision = 240 mm, slice thickness = 10 mm, matrix = 256 $\times$ 256), every 6 seconds/3 min in the midsagittal plane of the uterus. All images in 1 study were summated into 1 image and displayed sequentially on the cine mode display at 250-millisecond intervals. Subsequently, conventional axial and sagittal T_2-weighted images (TR/TE = 4000–4720/90–111 msec) and axial T_1-weighted images (TR/TE = 400–550/7.0–8.5 msec) were obtained to detect uterine myomas. One radiologist (T.H) interpreted the images without information about patients' menstrual cycles. Evaluation points included (1) perception of movement of the junctional zone on the cine mode display and (2) frequency of that movement, if perceivable. Patients were divided into 2 groups on the basis of the frequency of uterine peristalsis; less than 2 times/3 min (low-frequency group) and greater than or equal to 2 times/3 min (high-frequency group), as described [8].

Infertility treatments were performed as described [5]. Briefly, ovarian follicle growth was checked frequently, with transvaginal ultrasonography, in the absence of any drugs (natural cycle) or with clomiphene citrate or human menopausal gonadotropin for 2 to 3 courses, respectively. Clomiphene citrate (50–100 mg) was started on cycle day 5 for 5 days. Human menopausal gonadotropin was administered for 75 to 150 m IU on cycle day 3 and continued according to ovarian response. The size of the follicles was monitored until the diameter of the leading follicle reached 18 mm or greater, and the timing of ovulation was estimated. In some cases, human chorionic gonadotrophin at a dose of 5000 IU was administered. Intrauterine insemination was performed when motile sperm concentration was <20 $\times$ 10⁶/ mL. Luteal phase support was not performed. After the first MRI, the patients received infertility treatment at Teikyo University for at least 4 months before undergoing myomectomy.

In this study, 15 patients fulfilled the criteria. Of the 15 patients undergoing myomectomy, 1 case was an abdominal myomectomy, 7 cases were laparoscopic myomectomies, and 7 cases were laparoscopically assisted myomectomies, a procedure that used a small abdominal incision to remove the myomas. The patients' characteristics are summarized in Table 1. The infertility period shown in Table 1 is the timing when the first MRI was obtained. One patient (case 3 in

Table 1

Characteristics of patients and the findings of first MRI

Case	Age	Infertility	Infertility period (mo.)	Number of myomas	Maximum diameter (mm)
1	41	Sec	48	6	120
2	37	Prim	51	2	75
3	29	Sec	4	1	73
4	38	Prim	24	6	50
5	38	Sec	21	3	45
6	38	Prim	24	5	55
7	37	Prim	24	10	50
8	41	Prim	60	1	80
9	37	Sec	24	5	55
10	38	Prim	52	2	85
11	36	Prim	24	2	45
12	37	Prim	24	1	30
13	37	Prim	24	10	70
14	36	Prim	72	1	50
15	40	Prim	84	1	60

Prim = primary; Sec= secondary.

Fifteen infertility patients, who had intramural myomas and exhibited abnormal uterine peristalsis (≥ 2 times/3 minutes) in their first MRI, underwent myomectomy and a second MRI. Clinical characteristics, including age, primary or secondary infertility, the period of infertility (month), the number of myomas and the maximum diameter (mm) of myoma at their first MRI test are shown.

Table 1) visited our hospital and underwent the first MRI test at 4 months of her infertility period. She had severe hypermenorrhea and was refractory to the infertility treatment for 8 months; therefore she underwent myomectomy at 12

months of her infertility period. After the second MRI, which was obtained after myomectomy, patients resumed infertility treatment and continued for at least 8 months with the treatment strategy described above, with the exception of one patient who chose in vitro fertilization (IVF) treatment.

Data regarding age, number of myomas and maximum diameter of myomas were expressed as median with minimum-maximum range. The difference in pregnancy rate was analyzed by 2 × 2 contingency table analysis.

Results

The Effect of Myomectomy on Uterine Peristalsis

Fifteen patients with infertility who had intramural myomas and exhibited abnormal uterine peristalsis underwent myomectomy and a second MRI test. In the second MRI test, we confirmed that that all uterine myomas observed before surgery had been removed.

The frequency of uterine peristalsis was evaluated before and after surgery (Table 2). In patients who exhibited high peristalsis before surgery (≥ 2 times/3 min, n = 15), the uterine peristalsis was normalized in 14 patients (0 or 1 time/3 min), whereas 1 patient (case 11) continued to exhibit high uterine peristalsis (5 times/3 min before surgery, and 3 times/3 min after surgery).

Pregnancy after Myomectomy

After myomectomy and the second MRI, patients resumed infertility treatment for at least 8 months, and the

Table 2

Frequency of uterine peristalsis before and after surgery (per 3 minutes), surgical procedure, and pregnancy

Case	Peristalsis frequency (before surgery)	Peristalsis frequency (after surgery)	Operation	Pregnancy	Time to pregnancy (mo.)	Time of treatment (mo.)
1	6	0	Abdominal	YES	3	
2	6	1	LAM	YES	5	
3	4	1	LM	YES	4	
4	4	1	LAM	YES	1	
5	3	0	LAM	YES	2	
6	3	0	LAM	YES	4	
7	3	1	LAM	No		16
8	4	0	LM	No		15
9	3	1	LAM	No		13
10	4	0	LM	No		12
11	5	3	LM	No		11
12	4	0	LM	No		11
13	5	0	LAM	No		9
14	4	0	LM	No		8
15	2	0	LM	No		9

Abdominal = abdominal myomectomy; LAM = laparoscopically assisted myomectomy; LM = laparoscopic myomectomy.

Fifteen patients with infertility, who had intramural myomas and exhibited abnormal uterine peristalsis (≥ 2 times/3 minutes) in their first MRI, underwent myomectomy and a second MRI. The frequency of uterine peristalsis per 3 minutes before and after surgery is shown. The surgical procedure of abdominal myomectomy, laparoscopically assisted myomectomy, or laparoscopic myomectomy was shown. After myomectomy, the range of fertility treatment period (month) for both those who conceived (Yes) and those who did not (No) was shown.

pregnancy rate was evaluated (Table 2). Six of 15 patients achieved pregnancy (n = 15, pregnancy rate: 40%). In detail, 5 conceptions were achieved in a natural cycle, in which patients underwent ultrasonography to check follicular growth and received instruction with regard to the timing of intercourse (cases 1-5), and 1 case (case 6) was achieved with IVF techniques, which was done at an infertility clinic elsewhere. This patient had not attempted IVF techniques before undergoing myomectomy and did not try non-IVF treatment after the surgery. All 6 pregnancies were intrauterine and reached term. The birth rate was 6 of 15 patients (40%).

Discussion

During the implantation phase, it is well known that uterine peristalsis is dramatically reduced, which is believed to facilitate implantation of the embryo to the endometrium [8–10]. Using a cine mode MRI display, we have confirmed that no uterine corporal peristalsis was noted in the healthy volunteers during the mid- and late-luteal phases [7]. Furthermore, in the previous study, we found that less than half of the patients with intramural myomas exhibited abnormal uterine peristalsis during the mid-luteal phase. Interestingly, in the high-frequency peristalsis group, no patients achieved pregnancy, whereas one third of patients in the low-frequency peristalsis group achieved pregnancy in the presence of myomas [5]. These data suggest that abnormal uterine peristalsis caused by intramural myomas could be one of the factors causing infertility. To further examine this hypothesis, we investigated whether myomectomy for patients in the high-frequency peristalsis group is a constructive method to normalize uterine peristalsis. Here, we examined the same patients assessed in the previous study.

As shown in Table 2, myomectomy reduced the frequency of abnormal peristalsis in all patients, and the peristalsis rate returned to normal range (0 or 1 time/3 minutes) in 14 of 15 patients. Moreover, 6 of 14 patients achieved pregnancy after myomectomy.

A correlation between uterine peristalsis rates and pregnancy has previously been demonstrated [9,10]. With ultrasonography, Fanchin et al [9] examined the uterine peristalsis of patients with infertility who do not have uterine abnormalities and found a negative correlation between the frequency of uterine peristalsis on the day of embryo transfer and pregnancy outcome. These results suggest that high-frequency endometrial waves on the day of embryo transfer may negatively influence transfer outcome, perhaps by expulsion of the embryos from the uterine cavity [9].

Likewise, our previous data suggest that abnormal uterine peristalsis has a negative impact on implantation. In that study of 22 patients who exhibited high-frequency peristalsis, none achieved pregnancy (pregnancy rate; 0 of 22 patients [0%]) [5]. In this study, we found that myomectomy returned peristalsis rates to normal in these patients, with a subsequent increase in pregnancy rates (6 of 15 patients [40%]). Although there is a possibility of type I error because of the small sample

number, the pregnancy rate was improved significantly after surgery (p <.0012). Therefore these data might also suggest that abnormal uterine peristalsis has a negative impact on implantation.

In response to myomas, increased peristalsis may act as a mechanism to expel embryos from the uterus. Alternatively, estrogen is known to induce uterine peristalsis [11], and increased aromatase expression has been observed in uterine myomas [12]. Thus the elevated aromatase might result in elevated tissue estrogen concentration, which, in turn, could increase the rate of peristalsis. However, the precise mechanism by which myomas induce peristalsis remains unclear and requires further study.

In summary, we found that myomectomy reduced the frequency of uterine peristalsis in patients who had exhibited an abnormally high frequency of peristalsis before surgery. Moreover, we found that myomectomy increased the pregnancy rate in patients who had exhibited a high frequency of peristalsis. These findings suggest that the presence of uterine myomas might induce abnormal uterine peristalsis in some patients, leading to infertility, and that myomectomy may improve fertility in these patients.

Although the management of intramural type myomas continues to be difficult [1,2], cine mode MRI might have the potential to select patients who should undergo surgery. Because this study was preliminary, we made clinical decisions for the treatment of myomas not on the basis of the findings of cine mode MRI but on the traditional therapeutic strategy in which patients who were refractory to the infertility treatment had a choice to undergo myomectomy. Further randomized study with an increased number of subjects is warranted.

Acknowledgments

References

1. Donnez J, Jadoul P. What are the implications of myomas on fertility? A need for a debate? *Hum Reprod.* 2002;17:1424–1430.

2. Somigliana E, Vercellini P, Daguati R, Pasin R, De Giorgi O, Crosignani PG. Fibroids and female reproduction: a critical analysis of the evidence. *Hum Reprod Update.* 2007;13:465–476.

3. Richards PA, Richards PD, Tiltman AJ. The ultrastructure of fibromyomatous myometrium and its relationship to infertility. *Hum Reprod Update.* 1998;4:520–525.

4. Fujiwara T, Togashi K, Yamaoka T, et al. Kinematics of the uterus: cine mode MR imaging. *Radiographics.* 2004;24:e19.

5. Yoshino O, Hayashi T, Osuga Y, et al. Decreased pregnancy rate is linked to abnormal uterine peristalsis caused by intramural fibroids. *Hum Reprod.* 2010;25:2475–2479.

6. Ayres-de-Campos D, Silva-Carvalho JL, Oliveira C, Martins-da-Silva I, Silva-Carvalho J, Pereira-Leite L. Inter-observer agreement in analysis of basal body temperature graphs from infertile women. *Hum Reprod.* 1995;10:2010–2016.

7. Orisaka M, Kurokawa T, Shukunami K, et al. A comparison of uterine peristalsis in women with normal uteri and uterine leiomyoma by cine magnetic resonance imaging. *Eur J Obstet Gynecol Reprod Biol.* 2007;135:111–115.

8. Togashi K. Uterine contractility evaluated on cine magnetic resonance imaging. *Ann N Y Acad Sci.* 2007;1101:62–71.

9. Fanchin R, Righini C, Olivennes F, Taylor S, de Ziegler D, Frydman R. Uterine contractions at the time of embryo transfer alter pregnancy rates after in-vitro fertilization. *Hum Reprod.* 1998;13:1968–1974.

10. Fanchin R, Ayoubi JM. Uterine dynamics: impact on the human reproduction process. *Reprod Biomed Online.* 2009;18(Suppl 2):57–62.

11. Mueller A, Siemer J, Schreiner S, et al. Role of estrogen and progesterone in the regulation of uterine peristalsis: results from perfused non-pregnant swine uteri. *Hum Reprod.* 2006;21:1863–1868.

12. Bulun SE, Imir G, Utsunomiya H, et al. Aromatase in endometriosis and uterine leiomyomata. *J Steroid Biochem Mol Biol.* 2005;95:57–62.

Activin-A is induced by interleukin-1β and tumor necrosis factor-α and enhances the mRNA expression of interleukin-6 and protease-activated receptor-2 and proliferation of stromal cells from endometrioma

Osamu Yoshino, M.D., Ph.D.,[a,b] Gentaro Izumi, M.D.,[a] Jia Shi, M.D.,[a] Yutaka Osuga, M.D., Ph.D.,[a] Yasushi Hirota, M.D., Ph.D.,[a] Tetsuya Hirata, M.D., Ph.D.,[a] Miyuki Harada, M.D., Ph.D.,[a] Osamu Nishii, M.D., Ph.D.,[b] Kaori Koga, M.D., Ph.D.,[a] and Yuji Taketani, M.D., Ph.D.[a]

[a] Department of Obstetrics and Gynecology, University of Tokyo, Tokyo; and [b] Department of Obstetrics and Gynecology, Mizonokuchi Hospital, Teikyo University, Kawasaki, Japan

Objective: To examine the regulation and the function of activin-A in stromal cells derived from endometrioma.

Design: Molecular studies.

Setting: University research laboratory.

Patient(s): Endometrioma stromal cells (EoSC) were obtained from 28 patients with ovarian endometrioma undergoing laparoscopy.

Intervention(s): EoSC were cultured with inflammatory stimuli or recombinant activin-A, followed by RNA extraction.

Main Outcome Measure(s): Activin mRNA expression was evaluated by real-time reverse transcription–polymerase chain reaction (RT-PCR), and activin-A concentration of supernatant of cultured EoSC was evaluated by ELISA. Also, the effect of activin-A on EoSC was evaluated with real-time RT-PCR and cell proliferation assay.

Result(s): Inflammatory stimuli, interleukin (IL) -1β, and tumor necrosis factor (TNF) -α induced inhibin/activin-βA subunit mRNA and activin-A protein expression in EoSC. Additionally, activin-A enhanced EoSC proliferation and increased the expression of IL-6 and protease-activated receptor (PAR)-2 mRNA.

Conclusion(s): An in vitro study revealed that activin-A, which is induced by IL-1β or TNF-α, might promote endometriosis by stimulating IL-6 and PAR-2 mRNA expression and increasing the proliferation of EoSC. (Fertil Steril® 2011;96:118–21. ©2011 by American Society for Reproductive Medicine.)

Key Words: Endometriosis, activin-A, inflammatory cytokine, IL-6, PAR-2

Endometriosis is a gynecological condition in women of reproductive age, of which the primary symptoms are infertility and pain. Endometriosis is defined as the presence of viable endometrial glands and/or stroma outside of the uterine cavity. Although the etiology of endometriosis is unknown, multiple lines of evidence suggest that inflammation plays a pivotal role in the pathogenesis of the disease (1–4). We have shown that aberrant secretion of cytokines, such as interleukin (IL)-6, IL-8, and monocyte chemoattractant protein-1, in endometriotic tissue plays a role in modulating the inflammatory response. Moreover, we have demonstrated an association between protease-activated receptor (PAR)-2 and endometriosis.

PARs, which are members of the seven-transmembrane G-protein-coupled receptor family, are known to be important mediators of inflammation (5). We have reported that PAR-2 activation leads to the development of endometriosis by promoting endometrioma stromal cell (EoSC) growth and inflammation (6), while the formation of endometriotic lesions was suppressed in PAR-2 knockout mice (7).

Activins, which are a member of the TGF (transforming growth factor) -β superfamily, are homodimers of inhibin/activin-β subunits. Inhibins are heterodimers of inhibin-α and inhibin/activin-β subunits (8). Although activins are originally isolated as a factor that stimulates pituitary glands to secrete FSH (8), several studies provide evidence that activins also take part in inflammatory processes. For example, increased expression of activin-A has been shown in several inflammatory lesions, including ulcerative colitis, Crohn's disease, and interstitial pulmonary fibrosis (9, 10). Recent studies have demonstrated that activin-A and its receptors are expressed in endometriotic lesions (11, 12). Additionally, in vitro studies have demonstrated an increase in activin-A secretion from eutopic endometrium in women with endometriosis (12, 13).

These findings suggest that activin-A might be involved in the development and progression of endometriosis. However, the regulation of activin-A expression and its effect on the endometrium

is unknown. In the present study, we examined the regulation of activin-A expression in EoSC, focusing on inflammatory stimuli. Additionally, we examined the effect of activin-A on cultured EoSC.

MATERIALS AND METHODS
Reagents and Materials
Dulbecco's minimum essential medium (DMEM)/Ham's F12 (F12) medium, 0.25% trypsin-ethylenediaminetetraacetic acid (EDTA), and deoxyribonuclease I were from Invitrogen. Fetal bovine serum (FBS), type I collagenase, and antibiotics (mixture of penicillin, streptomycin, and amphotericin B) were purchased from Sigma. Recombinant human activin-A was from R&D Systems.

Patients and Samples
Tissue specimens were obtained from 28 patients with ovarian endometrioma undergoing laparoscopy after obtaining written informed consent under a study protocol approved by the Institutional Review Board of the University of Tokyo. All patients had regular menstrual cycles, and none had received hormone treatment for at least 3 months before surgery. Endometriotic tissue samples were obtained from the cyst wall of an ovarian endometrioma under sterile conditions and were histologically confirmed.

Isolation and Culture of Human EoSC
Primary EoSC culture was conducted as described elsewhere (14). Briefly, endometriotic tissue was dissected free of underlying parenchyma, minced into small pieces, incubated in DMEM/F12 with type I collagenase (2.5 mg/mL) and DNase I (15 U/mL) for 1–2 hours at 37°C, and separated using serial filtration. Debris were removed using a 100-μm nylon cell strainer (Becton Dickinson), and dispersed epithelial glands were eliminated with a 70-μm nylon cell strainer. Stromal cells remaining in the filtrate were collected by centrifugation, resuspended in DMEM/F12 with 10% charcoal-stripped FBS, penicillin (100 U/mL), streptomycin (100 μg/mL), and amphotericin B (250 ng/mL), and plated onto 100-mm dishes (Iwaki). When the cells became confluent after 2 days, they were dissociated with 0.25% trypsin, harvested by centrifugation, and replanted in 6-well plates at 2×10^5 cells/well. They were kept at 37°C in a humidified 5% CO_2/ 95% air environment until they were grown to confluence over the course of 2 days. Purification of the stromal cell population was confirmed by immunocytochemical staining for the following antibodies: vimentin (stromal cells), cytokeratin (epithelial cells), and CD45 (monocytes and other leukocytes). The purity of the stromal cell was more than 98%, as judged by positive cellular staining for vimentin and negative cellular staining for cytokeratin and CD45.

Treatment of Cultured EoSC
Cultured EoSC were treated with IL-1β (10 ng/mL; Genzyme) or tumor necrosis factor (TNF)-α (10 ng/mL; Genzyme) without FBS for 6 or up to 48 hours. In the experiment for mRNA expression, EoSC were cultured for 6 hours (n = 5). To examine the activin-A release into the medium, EoSC were plated to 12-well plates with 1 mL of DMEM/F12 with or without IL-1β or TNF-α. After incubation for 6, 24, and 48 hours, respectively, supernatants were collected and stored at −80°C until assay (n = 3). To examine the effect of activin-A on EoSC, cultured EoSC were stimulated with activin-A (0–300 ng/mL) without FBS for 6 hours to check mRNA levels. To examine the involvement of the activin receptor in activin-A-inducing responses in EoSC, SB431542 (10 μM), activin receptor–like kinase (ALK) -4, -5, and -7 inhibitor, or DMSO (control) was added 1 hour before activin-A stimulation (n = 3).

Reverse Transcription (RT) and Quantitative Real-Time Polymerase Chain Reaction (PCR) Analysis
Total RNA was extracted from EoSC, using the RNeasy minikit (Qiagen). RT was performed using Rever Tra Dash (TOYOBO). One microgram of total RNA was reverse transcribed in a 20-μL volume. For the quantification of various mRNA levels, real-time PCR was performed using LightCycler (Roche Diagnostic GmbH), according to the manufacturer's instructions. The PCR primers were selected from different exons of the corresponding genes to discriminate PCR products that might arise from possible chromosomal DNA contaminants. Especially, as activins are homodimers of inhibin/ activin-β subunits and inhibins are heterodimers of inhibin-α and inhibin/activin-β subunits (8), the mRNA of the inhibin-α subunit and the inhibin/activin-βA and -βB subunits was examined, respectively.

The primer sequences were as follows: inhibin-α subunit (NM_002191: 369–388 and 602–582), inhibin/activin-βA subunit (NM_002192: 505–526 and 673–653), inhibin/activin-βB subunit (NM_002193: 1184–1204 and 1325–1305), PAR-2 (NM_005242: 369–389 and 549–530), and GAPDH (NM_002046: 628–648 and 1079–1060). PCR conditions were as follows: IL-6, 40 cycles of 95°C for 10 seconds, 66°C for 8 seconds, and 72°C for 12 seconds; PAR-2, 40 cycles of 95°C for 10 seconds, 64°C for 10 seconds, and 72°C for 8 seconds; GAPDH, 35 cycles of 95°C for 10 seconds, 64°C for 10 seconds, and 72°C for 18 seconds; inhibin-α subunit, inhibin/activin-βA subunit, and inhibin/activin- βB subunit, 40 cycles of 95°C for 10 seconds, 55°C for 10 seconds, and 72°C for 8 seconds. After amplification, melting curve analysis was performed. Relative expression of each mRNA was normalized by GAPDH mRNA.

Cell Proliferation Assay
To examine the effect of activin-A on the cell number of EoSC, preconfluent EoSCs in 96-well plates were treated with vehicle (phosphate-buffered saline) or activin-A (100 ng/mL) in DMEM/F12 without serum for 48 hours. After 48 hours of stimulation, cell numbers were measured with a cell counting kit (CCK-8; Dojindo), based on the method of colorimetric assay. Briefly, media were replaced with DMEM/F12 without serum and 10 μL of the CCK-8 solution was added to each well and incubated for 1 hour in the incubator. Absorbance was measured at 450 nm using a microplate reader. The data were shown as a ratio to controls (mean ± SD) from four different experiments.

ELISA
The concentration of activin-A in supernatant was measured in triplicate using specific ELISA kits (Quantikine; R&D Systems). The sensitivity of the assay was 3.6 pg/mL. The intra-assay and interassay coefficients of variation were <5% in the assays. The data obtained were shown as a relative ratio to the basal level of 6 hours of culture.

Statistical Analysis
Data were analyzed by Student's t-test for paired comparison and one-way ANOVA with post hoc test for multiple comparisons using Statview software (SAS Institute Inc.). $P<.05$ was considered statistically significant.

RESULTS
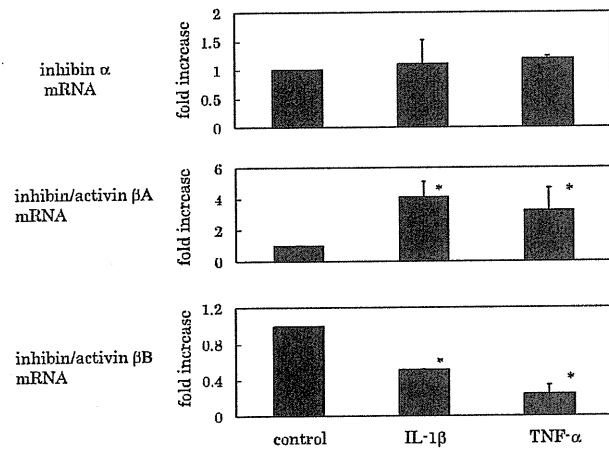### mRNA Expression of Inhibin/Activin Subunits in EoSC
As shown in Figure 1, with IL-1β and TNF-α stimulation for 6 hours, the inhibin-α subunit mRNA of cultured EoSC was unchanged. There was an approximately 3- to 4-fold (n = 5; $P<.01$) increase in inhibin/activin βA subunit mRNA expression with IL-1β or TNF-α stimulation compared with each control sample, while expression of the inhibin/activin-βB subunit was reduced by more than 50% with these stimuli (n = 5, $P<.01$).

Activin-A Concentration in Supernatant of EoSC
In EoSC, the basal level of activin-A release into the medium was increased in a time-dependent manner (Fig. 2). In the presence of IL-1β or TNF-α, the concentration of activin-A was over 3- to 5-fold higher than that of each control sample throughout the 48-hour culture period (n = 3; $P<.01$). Compared with IL-1β- and TNF-α-stimulated EoSC, IL-1β rather than TNF-α induced activin-A in cultured supernatant significantly throughout 48 hours ($P<.01$).

FIGURE 1

Inhibin/activin subunits mRNA in human EoSC. Cultured human EoSC were stimulated with IL-1β (10 ng/mL) or TNF-α (10 ng/mL) for 6 hours. Total RNA was extracted from the cells and subjected to real-time PCR to determine the inhibin/activin subunits mRNA levels. Data were normalized to GAPDH mRNA levels. Representative data from five different experiments were shown as the mean ± SEM relative to an adjusted value of 1.0 for the mean value of the each control. *P<.01 (vs. control).

Yoshino. The role of activin-A in endometriosis. Fertil Steril 2011.

FIGURE 3

The role of activin-A in EoSC. Cultured human EoSC were stimulated with activin-A (0–300 ng/mL) for 6 hours. SB431542 (10 μM), ALK-4, -5, and -7 inhibitor, or DMSO (control) was added 1 hour before activin-A stimulation. Total RNA was extracted from the cells and subjected to real-time PCR to determine the IL-6 and PAR-2 mRNA levels. Data were normalized to GAPDH mRNA levels. Representative data from three different experiments were shown as the mean ± SEM relative to an adjusted value of 1.0 for the mean value of the each control. *P<.01 (vs. control).

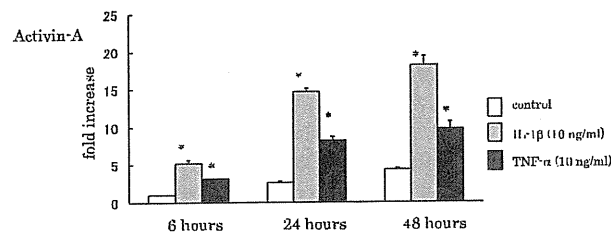*Yoshino. The role of activin-A in endometriosis. Fertil Steril 2011.*

The Role of Activin-A in EoSC

As shown in Figure 3, activin-A significantly induced IL-6 and PAR-2 mRNA expression of EoSC in a dose-dependent manner. Although IL-6 mRNA expression was induced significantly with activin-A at the concentration of 0.1 ng/mL, upregulation of PAR-2 mRNA expression was observed at 100 ng/mL (n = 3; P<.01).

In the presence of SB431542 (10 μM), ALK-4, -5, and -7 inhibitor, activin-A-induced IL-6, and PAR-2 expression was suppressed. Moreover, SB431542 reduced the basal level of PAR-2 but not IL-6 mRNA expression (n = 3; P<.01).
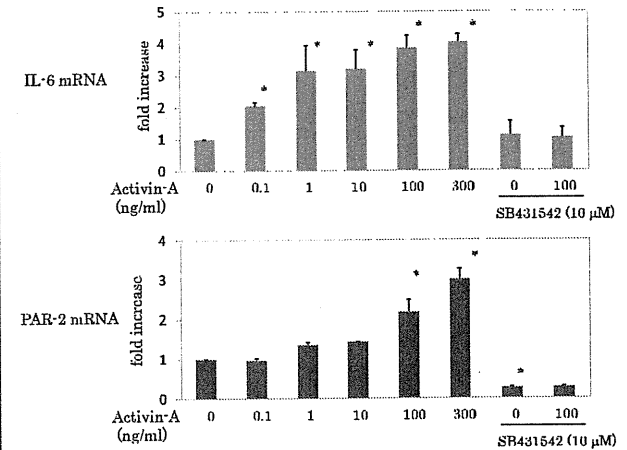
FIGURE 2

Activin-A concentration in the supernatant of EoSC. Cultured human EoSC were stimulated with IL-1β (10 ng/mL) or TNF-α (10 ng/mL) for 6–48 hours. Activin-A concentration in the supernatant of cultured EoSC was measured in triplicate by ELISA, and data were shown as a relative ratio to the basal level of 6 hours of culture. One representative data point from three different experiments were shown. *P<.01 (vs. control).

Yoshino. The role of activin-A in endometriosis. Fertil Steril 2011.

In a cell proliferation assay, activin-A (100 ng/mL) stimulation for 48 hours exhibited a significant 1.3-fold increase in the number of EoSC (n = 4, mean ± SD, 1.3 ± 0.02; P<.0001).

DISCUSSION

In the present study, we found that inflammatory stimuli IL-1β and TNF-α induced activin-A expression in EoSC. Activin-A also enhanced EoSC proliferation and the expression of IL-6 and PAR-2 mRNA.

It is likely that an altered immunoinflammatory environment in the peritoneal cavity supports the survival and growth of endometriotic lesions. A variety of cytokines and growth factors derived from activated macrophages, endometriotic cells, and mesothelial cells in the abdominal cavities of women with endometriosis are thought to play a role in the development of the disease (1–4). IL-1β and TNF-α in particular may be key molecules involved in the disease process (1). These cytokines elicit pleiotropic effects, such as stimulation of cytokine secretion and cyclo-oxygenase (COX)-2 expression (14).

In the present study, we found that IL-1β and TNF-α increased the expression of the inhibin/activin-βA subunit in EoSC, without changing the inhibin-α subunit level. Consistent with the increase in mRNA expression, activin-A protein levels in the cultured supernatant were also upregulated with these stimuli. These results might explain the high concentration of activin-A protein that has been observed in the peritoneal fluid of patients with endometriosis (15).

Interestingly, mRNA expression levels of the inhibin/activin-βB subunit were suppressed with inflammatory stimuli. This result is consistent with observations by Reis et al., who showed that ovarian endometriotic cells fail to express the inhibin/activin-βB subunit (15), and Florio et al., who demonstrated that the concentration of inhibin-B in the supernatant of cultured EoSC is less than that of

inhibin-A, suggesting that the inhibin/activin βA subunit is predominant in endometriotic tissue (16). The lower expression levels of the inhibin/activin-βB subunit in ovarian endometriotic cells could also be the result of inflammation.

We also examined whether activin-A augmented the proliferation of endometriotic cells. The effect of activins on cell proliferation is known to be cell dependent. Activins stimulate proliferation of cells of various origins, including lung fibroblast, keratinocyte, thyroid cells, osteoblasts, and spermatogonial cells, but also exhibit an antiproliferation effect on lymphocytes and prostate cancer cells (17). In the present study, activin-A induced proliferation of EoSC derived from endometrioma.

Furthermore, we found that activin-A induced expression of two known accelerators of endometriosis, IL-6 and PAR-2, in a dose-dependent manner. Dose-dependent studies revealed that IL-6 mRNA was induced at lower concentrations of activin-A compared with PAR-2 mRNA, suggesting the dose-dependent function of activin-A in the development of endometriosis. High IL-6 expression levels have previously been observed in the peritoneal fluid of women with endometriosis (18). Moreover, IL-6 secretion from endometriotic cells is a putative pathophysiological mechanism underlying the development of endometriosis (19). We also have shown that PAR-2 is involved in the pathogenesis of endometriosis (6, 7). Although the regulation of PAR-2 expression in EoSC has not been clarified, the present study revealed that activin-A could be an important factor in the regulation of PAR-2 expression. Notably, basal levels of PAR-2 but not IL-6 were reduced with the addition of SB431542, an inhibitor of several TGF-β family cytokines. This result suggests that cytokines of the TGF-β superfamily are likely to play a role in the regulation of the basal PAR-2 expression in EoSC.

In summary, we have demonstrated that activin-A is induced by inflammatory stimuli and then mediates the development of endometriosis by inducing cell proliferation and further increasing the inflammatory response.

REFERENCES

1. Lebovic DI, Mueller MD, Taylor RN. Immunobiology of endometriosis. Fertil Steril 2001;75:1–10.
2. Harada T, Iwabe T, Terakawa N. Role of cytokines in endometriosis. Fertil Steril 2001;76:1–10.
3. Kajihara H, Yamada Y, Kanayama S, Furukawa N, Noguchi T, Haruta S, et al. New insights into the pathophysiology of endometriosis: from chronic inflammation to danger signal. Gynecol Endocrinol 2011;27:73–9.
4. Gonzalez-Ramos R, Van Langendonckt A, Defrere S, Lousse JC, Colette S, Devoto L, et al. Involvement of the nuclear factor-kappaB pathway in the pathogenesis of endometriosis. Fertil Steril 2010;94:1985–94.
5. Cocks TM, Moffatt JD. Protease-activated receptors: sentries for inflammation? Trends Pharmacol Sci 2000;21:103–8.
6. Hirota Y, Osuga Y, Hirata T, Harada M, Morimoto C, Yoshino O, et al. Activation of protease-activated receptor 2 stimulates proliferation and interleukin (IL)-6 and IL-8 secretion of endometriotic stromal cells. Hum Reprod 2005;20:3547–53.
7. Osuga Y, Hirota Y, Taketani Y. Basic and translational research on proteinase-activated receptors: proteinase-activated receptors in female reproductive tissues and endometriosis. J Pharmacol Sci 2008; 108:422–5.

8. Ling N, Ying SY, Ueno N, Shimasaki S, Esch F, Hotta M, et al. Pituitary FSH is released by a heterodimer of the beta-subunits from the two forms of inhibin. Nature 1986;321:779–82.
9. Hubner G, Brauchle M, Gregor M, Werner S, Activin A. a novel player and inflammatory marker in inflammatory bowel disease? Lab Invest 1997;77:311–8.
10. Matsuse T, Ikegami A, Ohga E, Hosoi T, Oka T, Kida K, et al. Expression of immunoreactive activin A protein in remodeling lesions associated with interstitial pulmonary fibrosis. Am J Pathol 1996;148:707–13.
11. Mabuchi Y, Yamoto M, Minami S, Umesaki N. Immunohistochemical localization of inhibin and activin subunits, activin receptors and Smads in ovarian endometriosis. Int J Mol Med; 25:17–23.
12. Rombauts L, Donoghue J, Cann L, Jones RL, Healy DL. Activin-A secretion is increased in the eutopic endometrium from women with endometriosis. Aust N Z J Obstet Gynaecol 2006;46:148–53.
13. Torres PB, Florio P, Galleri L, Reis FM, Borges LE, Petraglia F. Activin A, activin receptor type II, nodal, and cripto mRNA are expressed by eutopic and ectopic endometrium in women with ovarian endometriosis. Reprod Sci 2009;16:727–33.

14. Yoshino O, Osuga Y, Hirota Y, Koga K, Hirata T, Harada M, et al. Possible pathophysiological roles of mitogen-activated protein kinases (MAPKs) in endometriosis. Am J Reprod Immunol 2004;52:306–11.
15. Reis FM, Di Blasio AM, Florio P, Ambrosini G, Di Loreto C, Petraglia F. Evidence for local production of inhibin A and activin A in patients with ovarian endometriosis. Fertil Steril 2001;75:367–73.
16. Florio P, Luisi S, Vigano P, Busacca M, Fadalti M, Genazzani AR, et al. Healthy women and patients with endometriosis show high concentrations of inhibin A, inhibin B, and activin A in peritoneal fluid throughout the menstrual cycle. Hum Reprod 1998;13:2606–11.
17. Chen YG, Lui HM, Lin SL, Lee JM, Ying SY. Regulation of cell proliferation, apoptosis, and carcinogenesis by activin. Exp Biol Med (Maywood) 2002;227:75–87.
18. Mahnke JL, Dawood MY, Huang JC. Vascular endothelial growth factor and interleukin-6 in peritoneal fluid of women with endometriosis. Fertil Steril 2000;73:166–70.
19. Akoum A, Lemay A, Paradis I, Rheault N, Maheux R. Secretion of interleukin-6 by human endometriotic cells and regulation by proinflammatory cytokines and sex steroids. Hum Reprod 1996;11:2269–75.